

Tubular Surface Segmentation for Extracting Anatomical Structures From Medical Imagery

Vandana Mohan*, *Student Member, IEEE*, Ganesh Sundaramoorthi, *Member, IEEE*, and Allen Tannenbaum, *Fellow, IEEE*

Abstract—This work provides a model for tubular structures, and devises an algorithm to automatically extract tubular anatomical structures from medical imagery. Our model fits many anatomical structures in medical imagery, in particular, various fiber bundles in the brain (imaged through diffusion-weighted magnetic resonance (DW-MRI)) such as the cingulum bundle, and blood vessel trees in computed tomography angiograms (CTAs). Extraction of the cingulum bundle is of interest because of possible ties to schizophrenia, and extracting blood vessels is helpful in the diagnosis of cardiovascular diseases. The tubular model we propose has advantages over many existing approaches in literature: fewer degrees-of-freedom over a general deformable surface hence energies defined on such tubes are less sensitive to undesirable local minima, and the tube (in 3-D) can be naturally represented by a 4-D curve (a radius function and centerline), which leads to computationally less costly algorithms and has the advantage that the centerline of the tube is obtained without additional effort. Our model also generalizes to tubular trees, and the extraction algorithm that we design automatically detects and evolves branches of the tree. We demonstrate the performance of our algorithm on 20 datasets of DW-MRI data and 32 datasets of CTA, and quantify the results of our algorithm when expert segmentations are available.

Index Terms—Blood vessels, branch detection, cingulum bundle, computed tomography angiogram (CTA), segmentation, shape, tubular surfaces, vessel trees.

I. INTRODUCTION

DETECTING and extracting anatomical structures from medical imagery are vital steps in the use of computers to aid in the diagnosis of disorders and pathologies. Deformable

models [1] have been widely used for extracting anatomical structures from medical imagery. Much research on deformable models has been conducted from incorporating image edge information [2], [3], to region statistics [4]–[7], to textural information [8]–[12]. Often in medical imagery, image information alone is not sufficient to detect structures of interest and therefore, many works [13]–[15] attempt to incorporate prior known information on the shape of the structure of interest into the deformable model extraction algorithm. This has been done in two ways: by creating penalties that penalize unfavorable shapes [15] or by creating explicit models of shape, using prior training data [7], [16]. The first approach, although less flexible in shape than a standard deformable surface, many times leads to the deformable surface becoming stuck in undesirable local minima of the underlying energy partly due to the large number of degrees-of-freedom of the surface. The second approach often provides too much restriction on the shape of the deformable surface (for example, in cases such as disease where the target structure is different than shapes of the training set), and requires training data, which in is unavailable in many cases. In this work, we define a model of a deformable surface that is flexible enough to capture tubular anatomical structures, which are of great interest to the medical community, however, not as flexible as a general deformable surface to easily become stuck in undesirable configurations. We are also able to model general tree-like tubular surfaces where each branch is tube-like, and devise a corresponding algorithm to extract such a surface from medical imagery.

We now summarize the organization of the paper. In Section II, we discuss two structures to which our tubular model applies: the cingulum bundle and blood vessels. We discuss the need for extracting these structures from imagery and prior work on their segmentation, as well as the novelty of our proposed framework. In Section III, we discuss the proposed tubular surface model in detail including the motivation for the model and the energies used for segmentation. The optimization approach is discussed in detail in Section IV. We give details on initialization methodology for the optimization scheme in Section V, and elaborate on a branch detection algorithm in Section VI for generalizing the extraction procedure to extract tubular trees. In Section VII, we present extensive experiments on extracting the cingulum bundle from diffusion-weighted magnetic resonance imaging (DW-MRI) brain data and vessel trees in computed tomography angiography (CTA) cardiac data. Finally in Section VIII, we make concluding remarks and present directions for future research.

Preliminary versions of this work have appeared in [17] and [18].

Manuscript received February 12, 2010; revised May 04, 2010; accepted May 08, 2010. Date of current version November 30, 2010. This work was supported in part by grants from the National Science Foundation (NSF), Air Force Office of Scientific Research (AFOSR), Army Research Office (ARO), as well as by a grant from the National Institutes of Health (NIH) (NAC P41 RR-13218) through Brigham and Women's Hospital. This work is part of the National Alliance for Medical Image Computing (NAMIC), funded by the NIH through the NIH Roadmap for Medical Research, Grant U54 EB005149. Information on the National Centers for Biomedical Computing can be obtained from <http://nihroadmap.nih.gov/bioinformatics>. *Asterisk indicates corresponding author.*

*V. Mohan is with the Schools of Electrical and Computer Engineering and Biomedical Engineering, Georgia Institute of Technology, Atlanta, GA 30332 USA (e-mail: vandana@gatech.edu).

A. Tannenbaum is with the Schools of Electrical and Computer Engineering and Biomedical Engineering, Georgia Institute of Technology, Atlanta, GA 30332 USA and also with the Department of Electrical Engineering, Technion-IIT, 32000 Haifa, Israel. (e-mail: tannenba@ece.gatech.edu).

G. Sundaramoorthi is with the Department of Computer Science, University of California, Los Angeles, CA 90095 USA (e-mail: ganeshs@ucla.edu).

Color versions of one or more of the figures in this paper are available online at <http://ieeexplore.ieee.org>.

Digital Object Identifier 10.1109/TMI.2010.2050896

II. ANATOMICAL STRUCTURES OF INTEREST AND PRIOR WORK

The proposed framework can be applied to extract any tubular branched structure from either scalar or vector-valued imagery. In this work, we focus on segmenting two anatomical structures: the Cingulum bundle (CB), which is of interest in the diagnosis of schizophrenia, and the human vasculature, which is of interest for studying disorders such as atherosclerosis. The subsequent sections discuss the physical description and anatomical significance of these structures as well as prior work in the areas of segmenting the respective structures. While it is outside the scope of this work to discuss other neural fiber bundles, we demonstrate that the proposed framework also applies to the external and internal capsules. For further information about these and other fiber bundles, interested readers are referred to [19].

A. Cingulum Bundle

The Cingulum Bundle is a 5–7 mm in diameter fiber bundle that interconnects all parts of the limbic system. It originates within the white matter (WM) of the temporal pole, and runs posterior and superior into the parietal lobe, then turns, forming a “ring-like belt” around the corpus callosum, into the frontal lobe, terminating anterior and inferior to the genu of the corpus callosum in the orbital-frontal cortex [19]. It consists of long, association fibers that directly connect temporal and frontal lobes, as well as shorter fibers radiating into their own gyri.

It is a *thin, highly curved* structure that consists of a collection of neural fibers, which are mostly disjoint possibly intersecting, roughly aligned and centered around a fiber. The collection of fibers approximately forms a tube-like structure. Because of its involvement in executive control and emotional processing, the CB has been investigated in several clinical studies, including studies of depression and schizophrenia. The CB and other fiber bundles can be imaged through a modality called diffusion weighted magnetic resonance imaging (DW-MRI). This is an image in which each voxel consists of a collection of numbers that can be used to determine the amount of diffusion of water in various directions. A tensor at each voxel can be associated with the collection of numbers, and such an image is called a diffusion tensor magnetic resonance image (DT-MRI). Previous studies of schizophrenia using DT-MRI demonstrated decrease of FA in anterior part of the cingulum bundle [20], [21], at the same time pointing to the technical limitations restricting these investigations from following the entire fiber.

The diffusion pattern in the CB varies in orientation and anisotropy smoothly along the structure, and it has a distinct diffusion pattern from surrounding areas of the brain (see Fig. 3 for a sagittal slice of the CB). The CB is challenging to segment because of inhomogeneity of its diffusion pattern *globally* and the noisy nature of DW-MRI makes it difficult to detect edges separating the CB from the rest of the image.

There has been much research in detecting and characterizing neural connections between brain structures in DW-MRI. Early methods for detecting fibers, i.e., *tractography*, are based on streamlines where the fiber path is constructed by following the direction of the principal eigenvector of diffusion tensors from an initial seed point, e.g., [22], [23]. These methods have been shown to perform poorly in noisy situations and they often terminate prematurely before the fiber ending. To alleviate these

problems, a number of works, e.g., [24]–[30], construct an optimal path between a starting and ending seed. The procedure is repeated to detect all fibers of a bundle.

In this work, we segment the entire fiber bundle as a volumetric region enclosed by a surface. It is typically difficult to segment the CB using standard active surface techniques, e.g., [31], [32], adapted to DW-MRI, since the DW-MRI of the brain are extremely noisy and contain many local features that could trap the active surface in unlikely configurations. Standard region-based techniques adapted to DW-MRI or DT-MRI, e.g., [33], are generally not applicable to the segmentation of the CB since the statistics of the DW-MRI inside the CB cannot be described by a few *global* parameters (e.g., mean). The Mumford–Shah energy extended to DT-MRI, [34], which assumes piecewise smooth image data inside the surface, is applicable to the CB. However, the assumption of smoothness outside the surface is not valid because of many different structures outside the brain with varying diffusion patterns. In [35], the authors perform segmentation of the CB by treating the problem as a voxel classification problem. An energy is formulated that is maximum when the estimated probability distributions of the classes are maximally separated (in the sense of entropy). The method, as the Mumford–Shah approach, assumes two distribution classes one for the foreground (the CB) and one for the background, which is multimodal and hence not well described by a Gaussian distribution as done in the work. Noticing that standard region-based techniques are not applicable to the CB, an edge-based active surface method for segmenting the CB is considered by [36]. However, the method is sensitive to the noise in the DW-MRI. The work [37] designs an energy on volumetric regions that incorporates “local region-based” information and a prior favoring regions that are close to an initially detected center-line curve. However, the energy is highly dependent on the correct placement of the detected center-line, which is often not exactly in the center of the CB. The work in [38] follows a template-based approach by aligning a deformable fiber-bundle model to the subject tensor field, which has significant improvements over tracking individual fibers.

B. Blood Vessels in Cardiac Imagery

Blood vessel extraction from imagery is vital to surgical planning and the diagnosis of cardio-vascular disorders such as atherosclerosis. There are several techniques based on deformable models for vessel extraction; however, they have limitations that are addressed in the proposed work. In [39], the authors evolve a 3-D curve to align it to the boundary of vessels determined by image edges; the method only provides a single curve in the vessel not the entire volumetric region. In [40], a flux-maximizing flow on curves/surfaces is constructed to align the curve/surface normal along the gradient direction of the image. To take into account the geometrical shape of a vessel, the authors of [41] construct a geometric shape prior to favor vessel-like structures and combine it with image region statistics to deform the curve/surface to capture the vessel. In [42], a method based on image histogram information is used to deform an initial vessel tree that was obtained by registration of the image to a pre-segmented reference image. The methods [40]–[42] do

not explicitly model the tubular nature of the vessel(s) to be detected. Therefore in [43], the authors model vessels as the envelope of a collection of spheres, thus having an explicit tube-like model for the vessel. The segmentation is performed based on a minimal path technique [44]. The centerline is detected without any additional effort in comparison to methods which process the segmentation to obtain a centerline (e.g., [45]). The drawback of the method of [43] is that it requires that the user inputs the endpoints of the vessel branch. There has also been work on modeling vessels as a combination of a center-line and a chosen cross-sectional shape ([46]–[48]). In [49], the center-line is modeled as a 1-D B-spline curve and a 3-D surface evolution approach is employed to fit the vessel wall along the curve. Similarly, [50] uses a 3-D active surface to model the vessel branch, with axial constraints applied, and [51] puts forth a level set-based approach with an initial centerline. Lesage *et al.* [52] provides an excellent review of lumen segmentation methods which combine models of vessel appearance and geometry with image features. Amongst the reviewed methods, we note the methods that are related to the proposed method in their use of intensity information and/or incorporation of shape (tubularity). These include the use of statistical distributions for modeling the intensity range of tissues of interest ([53], [54]), coupled appearance models that combine information about the intensity distributions of the tissue of interest and the background ([55], [56]), geometric models such as surface models of tubularity ([49]) and models of center-line and crosssection ([48], [57]).

The above works are of two forms: 1) vessels are represented by a general deformable surface allowing one to capture in particular tree-like vessel structures or 2) branches of the vessel are modeled by parametric cylinder-like tubes. The former has the disadvantage of having many degrees-of-freedom that the approach is susceptible to undesirable local minima and is computationally costly while the latter is not flexible enough in that it cannot explicitly deal with vessel branching.

C. Novelty of the Proposed Framework

In this work, we model the CB as a tubular surface and blood vessels as tubular trees. Since the tubular surfaces that we consider are determined by a center-line in 3-D space and a radius function defined at each point of the center-line (see Fig. 1), the extraction problem can be reduced to optimizing an energy defined on 4-D curves, which *significantly reduces the computational cost of the optimization procedure when compared to an unconstrained deformable surface*. A benefit of our approach is that the center-line is automatically obtained through the extraction process. This provides a skeleton of the vessel tree, which facilitates fly-through for visualization to gauge plaque deposits and stenosis in the vessel interior. Our method was inspired by the work of [43] in which the authors model vessels as tubular regions formed by the union of spheres along a center-line. Energies are constructed on 4-D curves that represent tubes, and these energies are globally minimized using the minimal path technique [44]. The energies we construct cannot be optimized using the minimal path technique since our energies are directionally dependent—they depend on the position of the 4-D

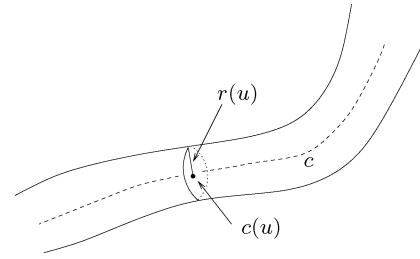


Fig. 1. Illustration of tubular surface model.

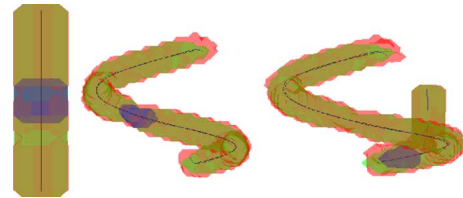


Fig. 2. Results of experiments with moving endpoints Implementation on synthetic imagery: the target structure (green), the segmentation result (red), the extracted center-line (black), the true centerline (blue), and the initial volume (blue). The first and second image are structures without branches, and the third image is a structure with a branch that our algorithm correctly detects.

curve and its *tangent*. Moreover, for the energies that we consider, we are not interested in a global minimum but rather certain local minima.

The advantage of our approach over existing methods in blood vessel extraction is that a model of the vessel tree that is general enough to capture entire vessel trees while having much fewer degrees-of-freedom than a general deformable surface alleviating susceptibility to undesirable local minima and keeping the computational cost low. We do this by proposing a tubular tree model and a corresponding automatic branch detection and evolution method that can be initialized by a single seed point. Other methods [39], [43], [49], [50] that use tube-like representations for the vessel can either deal with only a single branch or in order to capture multiple branches of the vessel tree, multiple seed points or initial regions for each individual branch must be chosen. Further, there is no guarantee that several of the tubes representing branches by the latter approach will not overlap in configurations that are unrealistic for vessel trees. While branch detection (in the blood vessel tree) has previously been addressed (e.g., [58], [59]), it is done after one has a segmented surface or skeleton.

III. BACKGROUND ON TUBULAR SURFACES

In this section, we define the tubular surfaces considered in this paper, and show that such a surface in \mathbb{R}^3 can be represented by a (1-D curve) in \mathbb{R}^4 . We formulate a general class of energies directly on curves living in \mathbb{R}^4 , and then describe the method to optimize these energies.

A. Proposed Model

We define a tubular surface as the boundary of a smoothly varying collection of discs (of varying radius) along a center line, which is an open curve in \mathbb{R}^3 . Given an open curve $c : [0, 1] \rightarrow \mathbb{R}^3$, the center line, and a function $r : [0, 1] \rightarrow \mathbb{R}^+$,

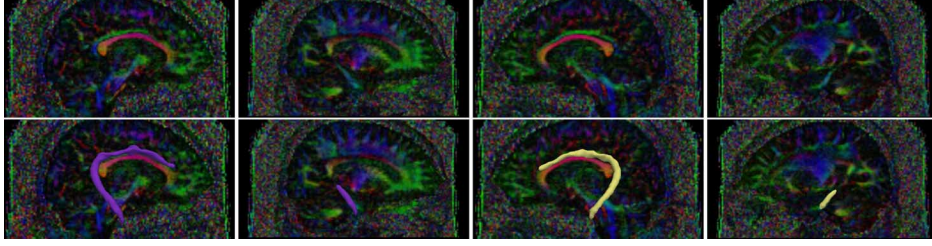


Fig. 3. Selected slice-wise views of CB Segmentation results from proposed framework (with fixed endpoints). The top row shows the DW-MRI data and the bottom row shows the DW-MRI data with the extracted surface rendered in 3-D.

the radius function, we can define the tubular surface, $S : \mathbb{S}^1 \times [0, 1] \rightarrow \mathbb{R}^3$ (\mathbb{S}^1 is $[0, 2\pi]$ with endpoints identified) as follows:

$$S(\theta, u) = c(u) + r(u)[n_1(u) \cos \theta + n_2(u) \sin \theta] \quad (1)$$

where $n_1, n_2 : [0, 1] \rightarrow \mathbb{R}^3$ are normals to the curve c defined to be orthonormal, smooth, and such that the dot products $c'(u) \cdot n_i(u)$ vanish. See Fig. 1 for an illustration of a tubular surface. The tubular surface is represented as a collection of circles each lying in the plane perpendicular to the center line. Note that the surface in (1) may be identified with a 4-D space curve, $\tilde{c} : [0, 1] \rightarrow \mathbb{R}^4$

$$\tilde{c}(u) = (c(u), r(u))^T. \quad (2)$$

B. Defining Energies for Segmentation

We now define a general class of energy functionals on the space of 4-D curves¹ (2) whose optimum represents the structure of interest, i.e., the CB from DW-MRI of the brain, or the blood vessel from CTA imagery of the cardiac region. Note that while we derive the expressions with respect to the structure of DW-MRI data (i.e., imagery in an oriented domain), the scalar CTA imagery can be thought of as a special case of imagery in an oriented domain with only one sampling direction.

Let $\mathbb{S}^2 \subset \mathbb{R}^3$ denote the unit sphere, which represents the set of all possible angular acquisition directions of the scanning device for DW-MRI. Let $I : \mathbb{R}^3 \times \mathbb{S}^2 \rightarrow \mathbb{R}^+$ be the diffusion image. We are interested in weighted length functionals on 4-D curves as energy functionals of interest. Indeed, let $\Psi : \mathbb{R}^4 \times \mathbb{S}^2 \rightarrow \mathbb{R}^+$ ($\Psi(x, r, v) \in \mathbb{R}^+$, where (x, r, v) defines a disc $D(x, r, v)$ of radius $r \in \mathbb{R}^+$ centered at point $x \in \mathbb{R}^3$, and $v \in \mathbb{S}^2$ is the normal to the disc) be a weighting function, which we call the *potential* to be chosen, and define the energy as

$$E(\tilde{c}) = \int_{\tilde{c}} \Psi(\tilde{c}(\tilde{s}), \frac{c'(\tilde{s})}{|c'(\tilde{s})|}) d\tilde{s}, \quad \tilde{c} = (c, r) \quad (3)$$

where $d\tilde{s} = |c'(u)| du = \sqrt{(r'(u))^2 + |c'(u)|^2} du$ is the ar-length measure of the 4-D curve, and $c'(\tilde{s})/|c'(\tilde{s})|$ is the unit tangent to c , the center line. When (3) is minimized, the term

¹In order for a 4-D curve to be associated with a tubular surface, the first three components, representing the center-line, must be such that it's derivative does not vanish. Further, the curvature of the center-line must be small compared with radii of the disc to ensure that the tube does not self-intersect.

$d\tilde{s}$ penalizes the nonsmoothness of the center line and the radius function. The energy (3) is related to the length of a curve in a Finsler manifold [60]–[62].

For segmenting the CB, the goal is to choose Ψ so that the energy is optimized by a \tilde{c} which determines a surface enclosing the diffusion pattern of the CB in the DW-MRI of the brain. The diffusion pattern in the cingulum varies in orientation and anisotropy across the length of the bundle, although being *locally* similar (see Fig. 3), and that pattern differs from the pattern immediately outside the CB. This fact precludes the use of traditional region-based techniques adapted to DT-MRI since these techniques assume homogeneous statistics within the *entire* region enclosed by the surface, whereas we will assume homogeneity within local regions. The idea is to choose Ψ at a particular coordinate (x, r, v) to incorporate statistics of the DW-MRI *local* to the disc determined by (x, r, v) rather than using statistics global to the entire structure as in traditional region based methods. For vessel segmentation, the potential, Ψ , is chosen to maximize the difference in mean intensities inside and outside the discs centered along the center-line. Again, the statistics employed are not global to the entire structure but rather local to the discs determined by (x, r, v) . In Sections III-C and III-D, we give examples of potentials that can be employed for the segmentation of the Cingulum Bundle and blood vessels, respectively.

C. Potentials for Segmenting the Cingulum Bundle

In this section, we give two choices for Ψ that are meaningful for extracting the CB from DW-MRI, both based on *local* region-based statistics.

The first potential Ψ_1 at a coordinate $(x, r, v) \in \mathbb{R}^3 \times \mathbb{R}^+ \times \mathbb{S}^2$ is constructed so as to be small when the *mean diffusion profile* inside the disc, $D(x, r, v)$, differs greatly from the mean diffusion profile inside the annular region, $D(x, \alpha r, v) \setminus D(x, r, v)$ where $\alpha > 1$, outside $D(x, r, v)$. This is given by the following expressions:

$$\Psi_1(x, r, v) = \frac{1}{1 + \|\mu_{D(x, r, v)} - \mu_{D(x, \alpha r, v) \setminus D(x, r, v)}\|^2} \quad (4)$$

where the $\mu : \mathbb{S}^2 \rightarrow \mathbb{R}^+$'s are the means (unto a constant multiple)

$$\mu_{D(x, r, v)}(\hat{v}) = \frac{1}{r^2} \int_{D(x, r, v)} I(\hat{x}, \hat{v}) dA(\hat{x}) \quad (5)$$

$$\mu_{D(x, \alpha r, v) \setminus D(x, r, v)}(\hat{v})$$

$$= \frac{1}{(\alpha^2 - 1)r^2} \int_{D(x, \alpha r, v) \setminus D(x, r, v)} I(\hat{x}, \hat{v}) dA(\hat{x}). \quad (6)$$

Here dA is the area element and $\|\cdot\|$ is a suitable norm on functions of the form $f : \mathbb{S}^2 \rightarrow \mathbb{R}^+$, e.g.,

$$\|f_1 - f_2\|^2 = \int_{\mathbb{S}^2} |f_1(v) - f_2(v)|^2 dS(v) \quad (7)$$

where dS is the surface area element of \mathbb{S}^2 . The energy corresponding to Ψ_1 is *minimized*. If it is desired to grow the tube from an initial seed point, the energy can be maximized using the potential $1/\Psi_1$.

Another example potential is chosen such that the corresponding energy is related to a weighted surface area

$$\begin{aligned} \Psi_2(x, r, v) &= r \int_0^{2\pi} \phi(x + rv^\perp(\theta)) d\theta \\ \text{and } v^\perp(\theta) &= n_1 \cos \theta + n_2 \sin \theta \end{aligned} \quad (8)$$

where n_1, n_2 are orthonormal vectors perpendicular to p , and $\phi : \mathbb{R}^3 \rightarrow \mathbb{R}^+$ is large near the boundary of differing diffusion regions, e.g.,

$$\phi(x) = \frac{1}{|B(x, R)|} \int_{B(x, R)} \|I(y, \cdot) - \mu_{B(x, R)}(\cdot)\|^2 dy. \quad (9)$$

Here $B(x, R)$ is the ball centered at x of chosen radius R , $|B(x, R)|$ denotes the volume, and the norm is defined as in (7). For this choice of potential, we are interested in *maximizing* the corresponding energy. The objective is to initialize the tubular surface inside the CB, and then increase weighted surface area until the surface reaches the boundary of differing diffusion patterns.

D. Potential for Vessel Segmentation

To maximize the difference in mean intensities inside and outside the discs centered along the center-line, the potential for vessel segmentation is given as

$$\Psi_3(x, r, v) = |\mu_{D(x, r, v)} - \mu_{D(x, \alpha r, v) \setminus D(x, r, v)}|^2. \quad (10)$$

As above the $\mu \in \mathbb{R}^+$'s are the means (up to a constant multiple)

$$\mu_{D(x, r, v)} = \frac{1}{r^2} \int_{D(x, r, v)} I(\hat{x}) dA(\hat{x}) \quad (11)$$

$$\begin{aligned} \mu_{D(x, \alpha r, v) \setminus D(x, r, v)} &= \\ &= \frac{1}{(\alpha^2 - 1)r^2} \int_{D(x, \alpha r, v) \setminus D(x, r, v)} I(\hat{x}) dA(\hat{x}). \end{aligned} \quad (12)$$

In the previous expressions, dA is the area element and $I : \mathbb{R}^3 \rightarrow \mathbb{R}^+$ is the scalar valued image representing the CTA. Notice that the energy (to be maximized) uses *local* region-based statistics to separate the tube's interior and exterior in comparison to traditional region-based approaches which separate the global mean intensities inside and outside the surface (e.g., [4]). It can thus be applied to vessel structures where the image intensity varies along the length of the vessel but approximately

constant in cross sections (not just vessels with a constant intensity profile).

IV. ENERGY OPTIMIZATION EQUATIONS

In this section, we construct a gradient flow to minimize/maximize the energy of interest (3).

A. Gradient Descent: Fixed Endpoints

In this subsection, we derive the gradient flow to minimize the energy (3). The flow is derived based on the constraint that the endpoints of the 4-D curve (i.e., the end discs of the tube) are fixed. The next section derives the equations for minimizing the energy by deforming the endpoints of the 4-D curve.

The standard technique for calculating the gradient of an energy defined on curves, which assumes a geometrized \mathbb{L}^2 metric on the space of deformations of a curve, cannot be applied to our energy of interest (3). This is because minimizing (3) stably using \mathbb{L}^2 requires Ψ must satisfy a positivity condition (see [62]) that cannot be guaranteed for our choices of Ψ . Moreover, maximizing (3), corresponds to maximizing a weighted length, which with respect to \mathbb{L}^2 , leads to an unstable reverse diffusion. As shown in [63], such weighted length functionals may be optimized in a *stable* manner by flowing along the gradient direction defined with respect to a *geometrized Sobolev metric*:

Definition: Let $\tilde{c} : [0, 1] \rightarrow \mathbb{R}^4$ be such that $\tilde{c}(0), \tilde{c}(1)$ are fixed. Let $h, k : [0, 1] \rightarrow \mathbb{R}^4$ be perturbations of \tilde{c} then

$$\langle h, k \rangle_{\mathbb{L}^2} := \frac{1}{L} \int_{\tilde{c}} h(\tilde{s}) \cdot k(\tilde{s}) d\tilde{s} \quad (13)$$

$$\langle h, k \rangle_{\text{Sob}} := L \int_{\tilde{c}} h'(\tilde{s}) \cdot k'(\tilde{s}) d\tilde{s} \quad (14)$$

where L is the length of the curve \tilde{c} , $d\tilde{s}$ is arclength element of \tilde{c} , and the derivatives are with respect to the arclength parameter \tilde{s} of \tilde{c} .

It can be shown that the gradient of (3) with respect to the Sobolev metric above (see Appendix A for a derivation) is

$$\frac{1}{L} \nabla_{\text{Sob}} E(\tilde{c}) = K(\Psi_p) + \partial_s K(\hat{\Psi}_v \sqrt{1 + \left(\frac{r\tilde{s}}{|c\tilde{s}|}\right)^2} + \Psi\tilde{c}_{\tilde{s}}) \quad (15)$$

where

$$K(f)(s) := \int_0^L K(s, \tilde{s}) f(\tilde{s}) d\tilde{s} \quad (16)$$

$$K(\tilde{s}_1, \tilde{s}_2) = \frac{1}{L} \begin{cases} \frac{\tilde{s}_2}{L} \left(1 - \frac{\tilde{s}_1}{L}\right) & 0 \leq \tilde{s}_2 \leq \tilde{s}_1 \\ \frac{\tilde{s}_1}{L} \left(1 - \frac{\tilde{s}_2}{L}\right) & \tilde{s}_1 \leq \tilde{s}_2 \leq L \end{cases} \quad (17)$$

$$\partial_s K(\tilde{s}_1, \tilde{s}_2) = \frac{1}{L^2} \begin{cases} 1 - \frac{\tilde{s}_1}{L} & 0 \leq \tilde{s}_2 \leq \tilde{s}_1 \\ -\frac{\tilde{s}_1}{L} & \tilde{s}_1 \leq \tilde{s}_2 \leq L \end{cases} \quad (18)$$

Ψ_p is the partial derivative of the energy function Ψ with respect to $p = (x, r)$, and $\hat{\Psi}_v = (\Psi_v, 0)^T$ where Ψ_v is the partial derivative with respect to orientation v .

Note that as stated in [63], the expression (15), in particular the expressions involving K , may be computed efficiently in

linear complexity with respect to the number of sample points of the curve (see Appendix A for details).

B. Evolving Endpoints

The previous section described how to evolve the 4-D curve to optimize the energy given that the endpoints remain fixed. We now derive the optimization procedure of the energy with respect to the endpoints. This is useful for some choices of Ψ in (3), for example, Ψ_2 and Ψ_3 defined in (8) where the idea is to grow the tube. To determine the evolution of the endpoints, we compute the variation with respect to the endpoints. This results in

$$\tilde{c}_t(0) = \mp \hat{\Psi}_v \sqrt{1 + \left(\frac{r_s}{|c_s|}\right)^2} \mp \Psi \tilde{c}_s \quad (19)$$

$$\tilde{c}_t(1) = \pm \hat{\Psi}_v \sqrt{1 + \left(\frac{r_s}{|c_s|}\right)^2} \pm \Psi \tilde{c}_s \quad (20)$$

which will minimize/maximize the energy (depending on the sign chosen above). Therefore, the algorithm to reduce the energy is to alternatively evolve the 4-D curve by (15) and the endpoints by (19) and (20).

V. INITIALIZATION AND OPTIMIZATION ALGORITHM

In this work, a gradient flow is used to optimize the energy of interest, and therefore the approach yields a local minimum (or maximum). The performance of this approach is sensitive to the initialization, of both the center-line and the cross-sectional radius of the tubular surface. For the segmentation of the CB from DW-MRI, we present two possible initialization schemes. Typically, seed points at the ending and beginning of the CB are given. If it is desired to incorporate both these points into the algorithm, it can be done by choosing those points to be the endpoints of an initial curve obtained by a traditional tractography algorithm (for example, we use the approach of [36], [60]–[62], but any other streamlining tractography approach can be used). This provides a rough estimate of a curve inside the CB, which can then be used to initialize the center-line of the 4-D curve, and the radius function can be initialized to 1 (the minimum radius). The optimization can then be performed using (15) and using potential Ψ_1 , keeping the endpoints of the 4-D curve fixed. We call this initialization/optimization the *Fixed Endpoint Implementation*. The other approach, called the *Moving Endpoint Implementation*, for initializing the tube for segmentation of the CB requires a seed point inside the CB around which a small tube (4-D curve) can be initialized. The energy (with potential Ψ_2) can then be optimized by alternating the evolution of the interior of the 4-D curve (15) and then the evolution of the endpoints (19) and (20).

In segmenting blood vessels from CTA imagery, we wish to segment an entire vessel tree comprising many branches modeled as tubular surfaces. It is not feasible to have the end points of each branch *a priori* and hence we only apply the moving endpoints approach (with potential Ψ_3) for blood vessel segmentation.

VI. BRANCH DETECTION

While we have modeled the Cingulum Bundle as a single tubular structure, in reality, it is a tubular structure encompassing discrete neural fibers, which further has branches that connect to surrounding gray matter regions in the brain. Blood vessels also have branching, and thus we describe in this section how to extend the tubular model to capture tubular trees. The branching nature of the structures of interest poses a challenge in applying the tubular surface segmentation framework directly, since we want to automatically detect branches in the vicinity of the evolving structure, as it grows out, and then construct new tube(s) to capture the detected vessel branches.

The proposed branch detection algorithm is summarized in Algorithm 1. The algorithm is based on the assumption that the vessels display greater intensity than their surrounding regions, and we perform the branch detection step each time an end point moves significantly (one voxel difference between its last location where a branch check was performed).

Algorithm 1 Branch detection algorithm Sample N directions $d_i \forall i \in (1, N)$ uniformly off the sphere \mathbb{S}^2 .

Construct tubes of radius 1 and length R along each of the N directions, originating at the end point under analysis.

Calculate the mean image intensity within each tube as $I_{mean}(d_i)$.

Threshold the estimated mean intensities with respect to the parent branch intensity I_{thres} .

Extract the subset of directions d_i with mean intensities above the threshold.

Apply k-means clustering [64], [65] to the extracted directions $d_i \forall i \in (1, N)$ and $I_{mean}(d_i) \geq I_{thres}$, with a target of 3 clusters.

if Number of non-empty clusters < 3 **then**

 Declare nonexistence of branching at end point under analysis

else

 Compute the centroid of the directions in each cluster, to yield 3 candidate branch directions.

 Eliminate the candidate direction that has maximum overlap with the parent branch's volume.

 Compute the dot products of the 2 remaining candidate directions with the tangent of the parent branch at the end point.

 Extend the parent branch by the candidate direction better aligned with the tangent at the end point.

 Create a new branch in the tree structure using the 1 remaining candidate direction.

end if

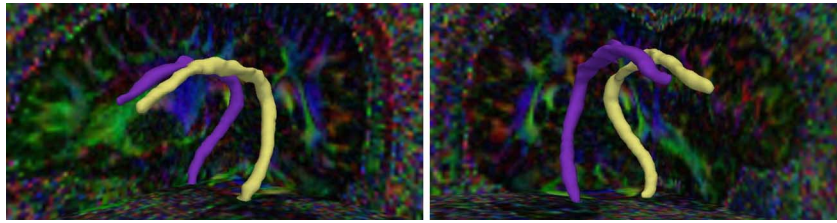


Fig. 4. CB Segmentation Results (with fixed endpoints) for Brain data set 1: Left CB (yellow), Right CB (magenta).

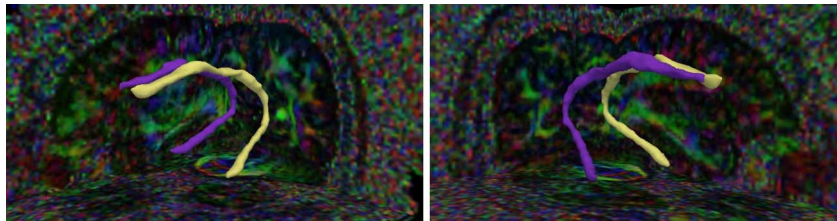


Fig. 5. CB Segmentation Results (with fixed endpoints) for Brain data set 2: Left CB (yellow), Right CB (magenta).

VII. EXPERIMENTS AND RESULTS

In this section, we begin by testing the framework on synthetic imagery to validate its performance on known ground truth. We then apply the proposed framework to extract the Cingulum Bundle from DW-MRI and then blood vessel trees from CTA. To test the algorithm in CB segmentation, it was applied to a DW-MRI data set that included schizophrenic and normal control subjects, with the DW-MRI being acquired for 54 sampling directions. The results were compared qualitatively with the results from the neural fiber bundle segmentation framework of Melonakos *et al.* [37], [62]. The experiments to demonstrate the use of the algorithm in blood vessel segmentation were conducted on a CTA data set that included data from healthy subjects (with no plaque) as well as subjects with varying degrees of plaque and stenosis. The framework was also tested on the Rotterdam CTA data set [66], and quantitative validation is provided.

A. Synthetic Imagery

In this set of experiments, the proposed framework was applied to both scalar and vector synthetic images with various curvilinear branched structures. Both the implementations of the algorithm were tested on these synthetic images. Fig. 2 shows the ground truth, segmentation results and associated center-line for the experiments with the Moving Endpoint implementation of the algorithm on the synthetic vector imagery. On average, the set-symmetric difference of the result with respect to ground truth was found to be $\sim 4\%$ across different synthetic structures of average radius 3 voxels.

B. CB Segmentation With Fixed Endpoints

The DW-MRI imagery used in this work was acquired on a 3T magnet using an echo planar imaging (EPI) DTI Tensor sequence with a double echo option to reduce eddy-current related distortions with eight baseline scans and data acquired in 51 directions. The population comprised 20 male subjects (10 normal, 10 schizophrenic) spanning the age group of 21–55

years. In this section, we show the results of applying the Fixed Endpoints implementation of the proposed framework to brain imagery of two subjects from this population. We use the energy (3) using the potential Ψ_1 (4). Fig. 3 shows slice-wise views of the CB segmentation results obtained from the proposed framework indicating the homogeneity of the discs within the captured volume. Figs. 4 and 5 show the tubular surface extracted by the proposed algorithm. The surfaces are shown in Fig. 3 are the boundary locations rounded off to the grid points by the visualization process.

With regard to the parameter α , the ratio between the outer and inner discs of the tube, we conducted experiments using a range from 2 to 5. We observed that as this value increases, the statistics for outside the disc are averaged over a larger area thus rendering them decreasingly effective in separating intensities within the tube and just outside it. For instance, with a value of α larger than 4, saw that the captured volume begins to leak into neighboring structures with strong diffusion such as the Corpus Callosum. From these initial experiments, we observed that a value of 3 yielded the most optimal results, with respect to leaking into the Corpus Callosum, and hence we used this in subsequent experiments.

C. CB Segmentation With Moving Endpoints

The Moving Endpoints implementation for CB segmentation, requires seed points in the interior of the CB near the start along with a guess for the initial radius. We applied the framework to segment the left and right Cingulum Bundle from all 20 data sets in the population under study (however, all visualizations cannot be presented in this paper). Figs. 6 and 7 show the results of applying the Moving Endpoints implementation to segmenting the CB (both right and left) from brain data of two subjects (one normal and one schizophrenic).

Fig. 8 shows the 3-D visualization of the segmentations obtained for the Cingulum bundle and other tubular fiber bundles, i.e., the External Capsule and the Internal Capsule.

Finally, we observe that quantitative studies are not possible in neural fiber bundle analysis due to the absence of ground

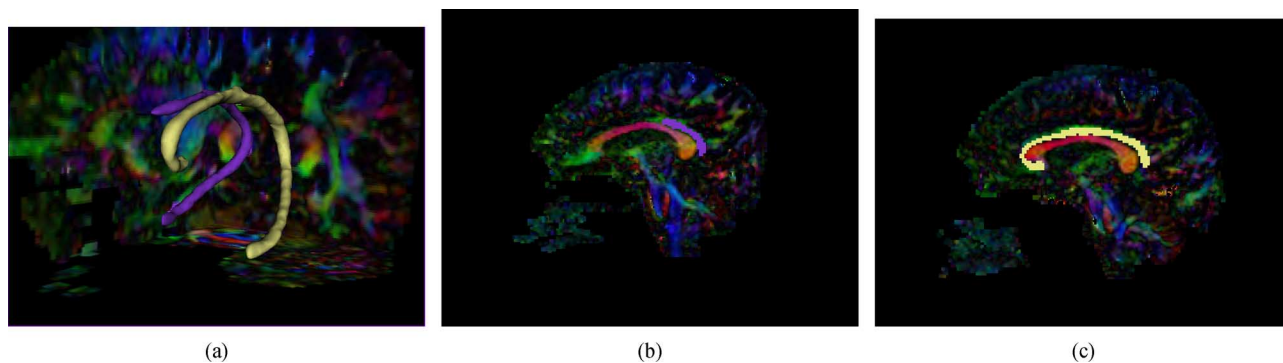


Fig. 6. CB Segmentation results (with moving endpoints) for Brain data set 3: Left CB (yellow), Right CB (magenta). (a) 3-D visualization. (b), (c) Slice-wise views.

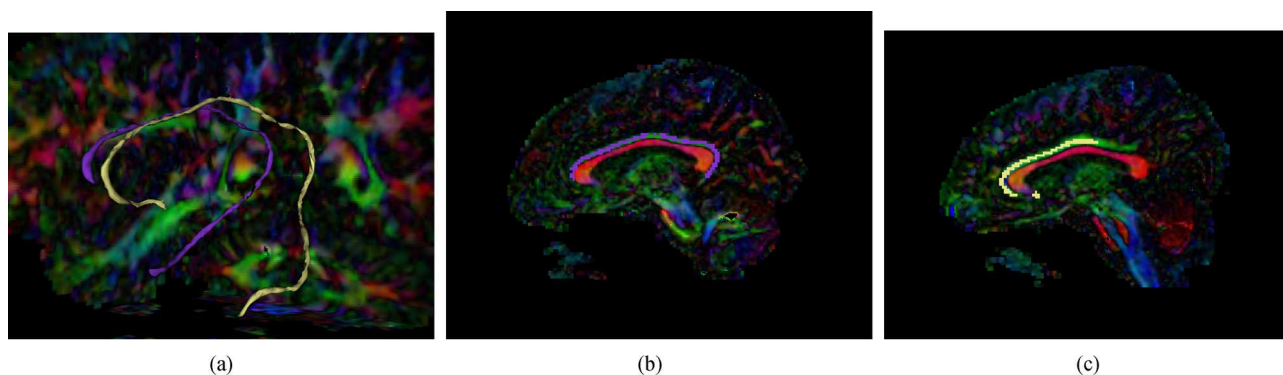


Fig. 7. CB Segmentation results (with moving endpoints) for Brain data set 4: Left CB (yellow), Right CB (magenta). (a) 3-D visualization. (b), (c) Slice-wise views.

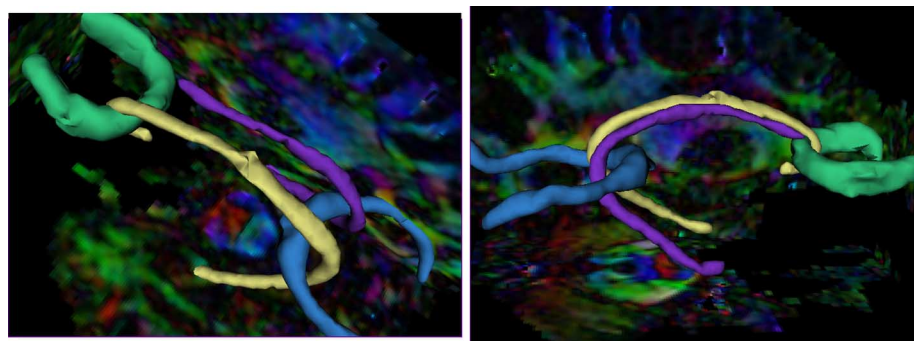


Fig. 8. 3-D Visualization of segmentation results showing usefulness of framework (with moving endpoints) for multiple fiber bundles: Left CB (yellow), Right CB (magenta), Internal Capsule (green), External Capsule (dark blue).

truth. However, we compare the results of the proposed framework with the results of the Geodesic Tractography Segmentation framework ([36], [37]). This comparison is provided in Fig. 9. Note that the proposed framework outperforms [36], [37] in some key ways. Firstly, due to the lack of constraints on the end points, the proposed framework extracts the neural fiber bundle to its true length as observed by diffusion patterns rather than being limited by the approximate ROIs provided by experts. Secondly, since the method enforces the tubular geometry as it propagates outwards, it is more robust to noisy data. This is especially highlighted by the fourth case (fourth row) in Fig. 9, where [36], [37] leaks into the Corpus Callosum while the proposed framework does not leak. It is also worth noting that the

CB extracted by the proposed framework passes through exactly the ROIs defined by the experts, which is further validation of the accuracy of the segmentation result.

Finally, it is to be noted that the Tubular Surface model is especially advantageous for neural fiber bundle analysis since the model naturally allows sampling of features along the length of the fiber bundles, which is simultaneously useful both in performing population studies on the neural fiber bundles, as well as characterizing the discrimination ability of local regions of the fiber bundles. This is demonstrated in the context of Schizophrenia detection in the work of Mohan *et al.* [67] and the interested reader can find details on the population analysis framework therein.

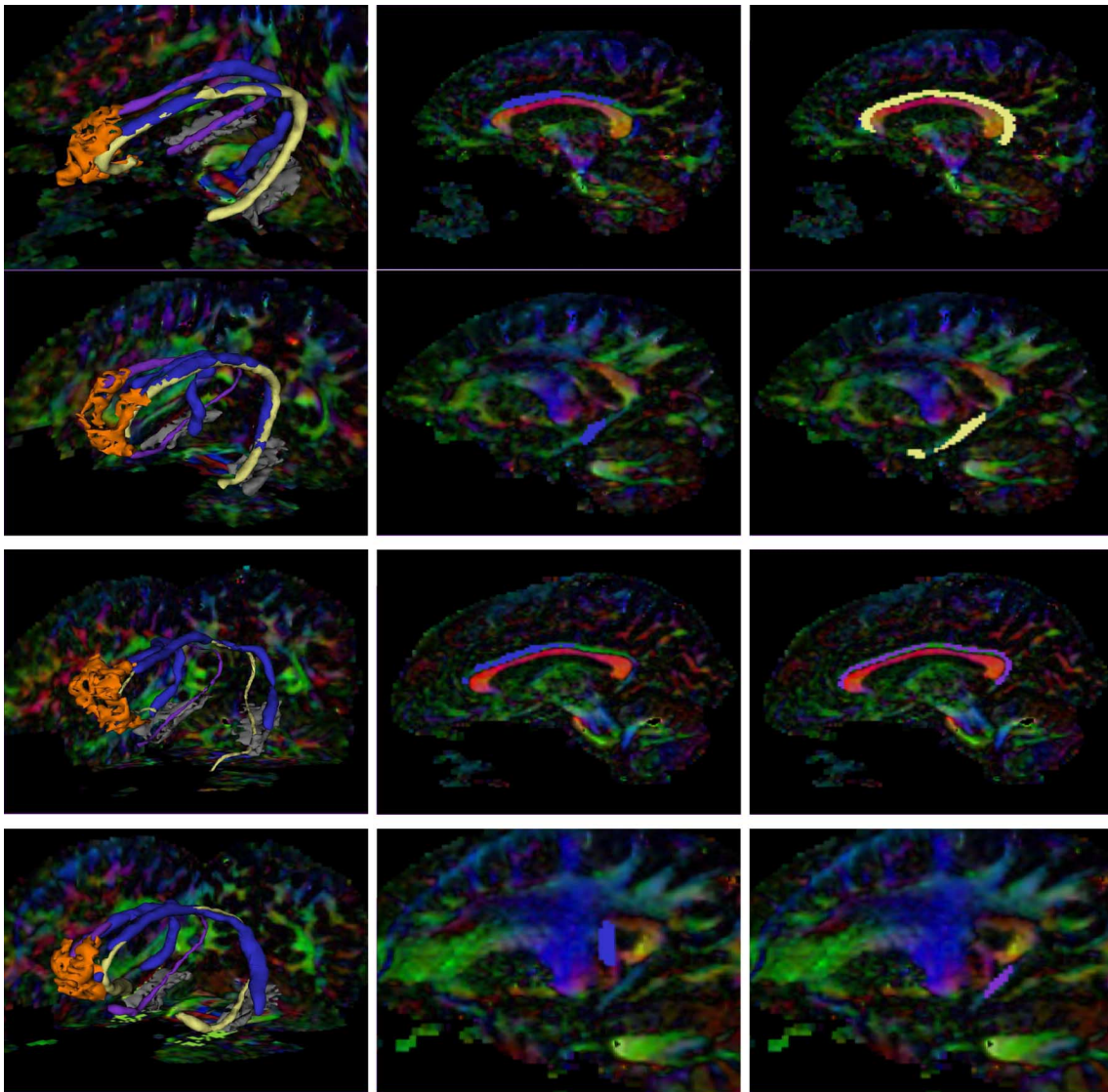


Fig. 9. Visual comparison of results from proposed framework with the framework of Melonakos *et al.* [36]: CB segmentation results from [36], [37] (blue), Left CB segmentation from proposed framework (yellow), Right CB segmentation from proposed framework (magenta), expert ROI markings for Rostral Anterior Cingulate (orange) and Parahippocampal gyrus (grey); Each row represents DW-MRI from a different subject, with the first two rows representing data from schizophrenic subjects, and the last two from normal controls. The first column shows the 3-D visualization of the extracted CB for both frameworks, and the expert-marked ROIs used as input for [36]. The second column shows a slice visualization of the fiber bundle extracted (for one side) by the framework of [36] and the third column shows the same view for the proposed framework, both superimposed on the tensor data. Note that the results from [36] are limited by the input ROIs and leak into neighboring fiber bundles (note the fourth row), while the proposed framework follows the true diffusion pattern hence capturing greater lengths of the fiber bundles, and it does not leak into neighboring structures.



Fig. 10. 3-D Visualization of the vessel tree for Case 1: segmentation result (red), center-line (green), initialization (blue).

D. Blood Vessel Segmentation

We apply the moving endpoints implementation to vessel segmentation, because it only requires a seed point for initialization

in a single branch. With regard to the parameter α , the ratio between the outer and inner disc radii, we conducted initial experiments using a range from 2 to 5. We observed that as this value increases, the statistics for outside the disc are in fact being averaged over a larger area thus rendering them decreasingly effective in separating intensities within the tube and just outside it, while a lower value rendered the functional more likely to be affected by noise. From these initial experiments, we observed that a value of 3 yielded good results and hence we have used this in subsequent experiments.

The algorithm was first tested on a population of cardiac data sets acquired from a Siemens Sensation 64 slice CTA machine. The framework was initialized with 1 user-input point at the root of the vessel tree, and a guess for typical vessel radius which guided the branch detection process.

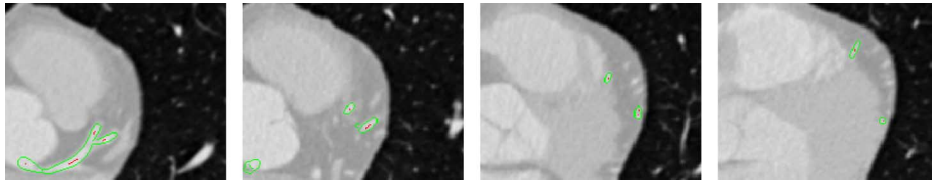


Fig. 11. Slice-wise views of the vessel segmentation result for Case 1.

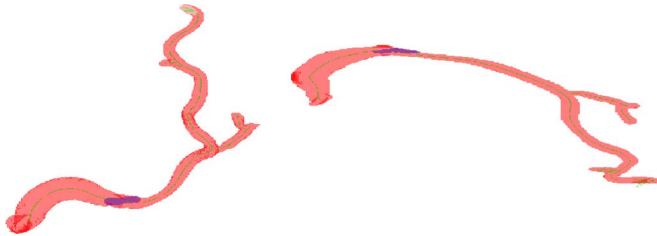


Fig. 12. 3-D Visualization of the vessel tree for Case 2: segmentation result (red), center-line (green), initialization (blue).

We first show here the results for three of the data sets tested on, for the Left Anterior Descending (LAD) coronary artery. Figs. 10 and 12 show the 3-D visualization of the segmented vessel trees for two cases. Also shown in these figures is the extracted center-line. The algorithm captures the branching structure automatically and successfully handles the thinning structure of the vessel tree, from the root to tips. Figs. 11 and 13 show the corresponding slice-wise views of the segmentation result. We can clearly see that the framework copes well with the nonuniform contrast within the vessel volume, and is capable of following an entire vessel ~ 200 voxels in length, from the simple one-point input used for these CTA datasets. Finally in Fig. 14, we show the tubular tree evolving in 3-D for a third case, illustrating how the branch detection works to capture the entire tree. These results have been qualitatively validated by medical collaborators.

We have performed quantitative validation via testing on the dataset provided as part of the Rotterdam Coronary Artery Algorithm Evaluation Framework [66]. The proposed segmentation framework was applied to all 32 datasets available via this dataset (including the training and testing data sets), and the results were submitted to the organizers for extracting the evaluation parameters. Table I gives the summary of the evaluation parameters obtained: OV that quantifies the tracking/overlap of the complete vessel as annotated by the human experts, OT that quantifies the tracking of the portion of the vessel that is assigned to be clinically relevant by experts, OF that quantifies the tracking of a coronary artery until the first error and AI, an accuracy measure of centerline extraction, which is the average of all the connections between the ground truth and the extracted centerline. We observe that the framework yields comparable results to the methods evaluated in [66], which also provides more detailed definitions of the evaluation parameters employed in this work. Also, we note that the proposed framework fits into Category 3 of evaluated methods as per the classification of [66] since we use more than one input point for the vessel segmentation from this data set (an average of 3–5 input

points are employed per subject for this data set). Finally, we note that along with yielding good performance, the proposed method also compares favorably with the methods evaluated in [66], notably in not needing to be trained for its use in the segmentation of real data along with its use of a limited number of initial points. Further, as compared to the other methods, the proposed framework simultaneously detects both the volume in 3-D as well as the center-line of the vessel structure. Figs. 16 and 17 show visualizations for the results of two cases from this dataset.

A potential application of our framework is stenosis evaluation. Since the 3-D skeleton and the associated radius function are direct outputs of the model, we can do a stenosis evaluation by looking for local minima of the radius function along the center-line. We show proof-of-concept of this idea in Fig. 15 which shows the cross-sectional area of one of the branches of the extracted vessel tree shown in Fig. 10 and reveals a site of mild stenosis (40% blockage) (corresponding to the minimum of the plotted curve).

VIII. CONCLUSION

In this work, we proposed a framework for extracting tubular, branched anatomical structures that *simultaneously returns the segmented volume and the 3-D skeleton of the structure of interest*. We showed that our methodology is successful in segmenting structures of interest from imagery of different modalities especially on the Cingulum Bundle from DW-MRI of the brain and blood vessels from cardiac CTA imagery. We demonstrated the generality of the framework by applying it to the segmentation of other neural fiber bundles (the Internal Capsule and the External Capsule). We also proposed an automatic branch detection algorithm which we have successfully applied to the segmentation of entire blood vessel trees. The incorporation of local region-based statistics implies that the segmentation result captures regions with statistics that can differ over the length of the entire structure. This is clearly illustrated by the performance of the framework in capturing the entire CB where diffusion patterns vary along the length of the tube, and again in segmenting the entire length of blood vessels where the contrast varies along each vessel. Further, the model affords us the advantage of computational efficiency over conventional surface representations.

In future work, we plan to apply the framework into segmenting other tubular anatomical structures that are of interest such as carotids in the brain, and veins in the liver region, and also study in greater detail the other neural fiber bundles. It is also of interest to use the extraction of fiber bundles through our algorithm for population studies to attempt to discriminate between normal and schizophrenic patients. Further, with respect

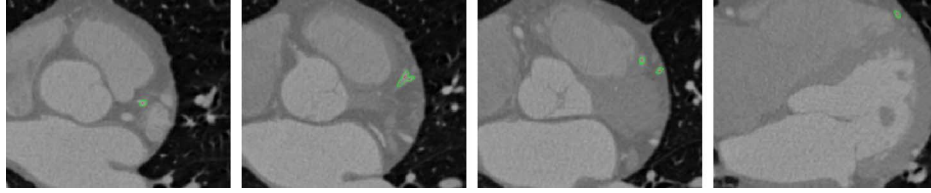


Fig. 13. Slicewise views of the vessel segmentation result for Case 2.

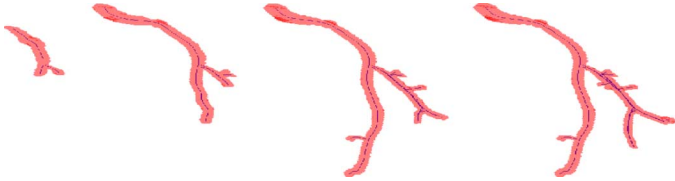


Fig. 14. Visualization of the evolving tubular tree in 3-D for Case 3: evolving volume (red), center-line (blue). Note that the framework captures the entire length ~ 200 voxels of the vessel starting from a simple initialization.

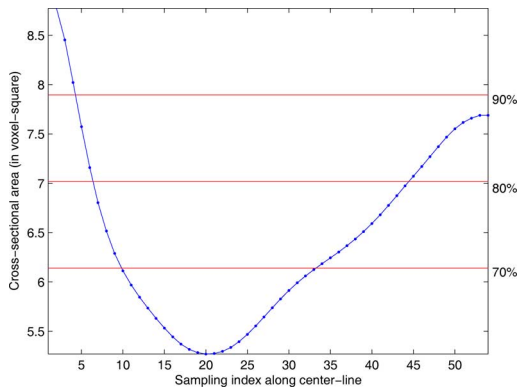


Fig. 15. Cross-sectional area along vessel shown in Fig. 10. The left y-axis shows the cross-sectional area in voxel-square and the red lines highlight the values of area that correspond to stenosis percentages displayed on the right y-axis. Note that the minimum of this curve indicates area of mild stenosis.

to the analysis of blood vessels, we propose to apply the proposed framework in soft plaque detection and explore its potential in evaluating stenoses.

APPENDIX

DERIVATION OF TUBULAR SURFACE EVOLUTION

In this section, we provide the detailed derivation of the evolution equations for the proposed Tubular Surface model.

Sobolev Gradient in Terms of the \mathbb{L}^2 Gradient: We begin by expressing the Sobolev gradient as a function of the standard \mathbb{L}^2 gradient, which can be using standard variational calculus. Let $\Gamma : [0, 1] \rightarrow \mathbb{R}^d$ ($d = 3$ or $d = 4$) define a space curve such that $\Gamma(0) = \Gamma_0$ and $\Gamma(1) = \Gamma_1$ where $\Gamma_0, \Gamma_1 \in \mathbb{R}^d$ are the fixed endpoints of Γ . Let E be an energy defined on Γ , and let $g = \nabla_{\text{Sob}} E$, $f = \nabla_{\mathbb{L}^2} E$ denote the Sobolev and \mathbb{L}^2 gradients of E , respectively.

By the definition of the inner products (13) and (14), g and f are related as follows:

$$-L^2 g_{ss} = f, \quad g(0) = g(L) = 0 \quad (21)$$

where s represents the arclength parameter of Γ , L is the length of Γ , and the boundary condition corresponds to endpoints that are to be fixed during evolution. Equation (21) can be solved for g by integrating yielding

$$g'(s) = g'(0) - \frac{1}{L^2} \int_0^s f(\hat{s}) d\hat{s} \quad (22)$$

integrating again yields

$$\begin{aligned} g(s) &= g(0) + sg'(0) - \frac{1}{L^2} \int_0^s \int_0^{\hat{s}} f(\epsilon) d\epsilon d\hat{s} \\ &= sg'(0) - \frac{1}{L^2} \int_0^s f(\hat{s})(s - \hat{s}) d\hat{s} \end{aligned} \quad (23)$$

where

$$g'(0) = \frac{1}{L^3} \int_0^L f(\hat{s})(L - \hat{s}) d\hat{s}. \quad (24)$$

The expressions (23) and (22) above yield a linear complexity (in the number of sample points of Γ) computational algorithm for computing g in terms of f .

Since the transformation mapping f to g is a bounded linear operator, it can be expressed as an integral operator, i.e.,

$$g(s) = \int_0^L K(s, \hat{s}) f(\hat{s}) d\hat{s} =: K(f)(s) \quad (25)$$

where s, \hat{s} are arclength parameters of Γ , $K : [0, L]^2 \rightarrow \mathbb{R}$ is a symmetric kernel, and by abuse of notation, we also write $g = K(f)$ to denote the linear operator defined above. By manipulation of (23) and (22), one can find that K is given as in (17). Note also that

$$g'(s) = \int_0^L \partial_s K(s, \hat{s}) f(\hat{s}) d\hat{s} =: (\partial_s K)(f)(s). \quad (26)$$

The expressions (25) and (26) are for simplicity of notation and ease of mathematical manipulation in the subsequent computations. However, for numerical implementation the expressions (25) and (26) are computed using the expressions (23) and (22), as doing so results in lower computational complexity.

Sobolev Gradient of Tubular Energy: We begin by computing the \mathbb{L}^2 gradient of the tubular energy (3). Let $\tilde{c} : [0, 1] \rightarrow \mathbb{R}^4$ and $\tilde{c} = (c, r)$ where $c : [0, 1] \rightarrow \mathbb{R}^3$ is immersed and $r : [0, 1] \rightarrow \mathbb{R}^+$. Denote by s in this subsection, the arclength parameter of c , by \tilde{s} the arclength parameter of \tilde{c} , and by $u \in [0, 1]$ a parameter of a parameterization of \tilde{c} . Then (3) can we written

$$E(\tilde{c}) = \int_0^1 \Psi(\tilde{c}(u), \frac{c'(u)}{|c'(u)|}) |\tilde{c}'(u)| du$$

TABLE I
SUMMARY OF QUANTITATIVE VALIDATION RESULTS ON CTA CARDIAC DATA FROM THE ROTTERDAM CORONARY ARTERY ALGORITHM EVALUATION FRAMEWORK [66] (IT IS DESIRABLE TO HAVE A HIGH VALUE OF EVALUATION PARAMETERS OV, OF, OT, AND AI, AND A LOW VALUE OF RANK)

Measure	% / mm			score			rank		
	min.	max.	avg.	min.	max.	avg.	min.	max.	avg.
OV	52.8%	100.0%	91.1%	28.0	100.0	53.3	1	16	8.73
OF	4.6%	100.0%	65.3%	2.3	100.0	41.9	1	16	8.15
OT	52.8%	100.0%	92.2%	26.5	100.0	53.9	1	16	8.83
AI	0.25 mm	0.93 mm	0.47 mm	12.4	48.8	24.8	5	16	12.90
Total							1	16	10.73

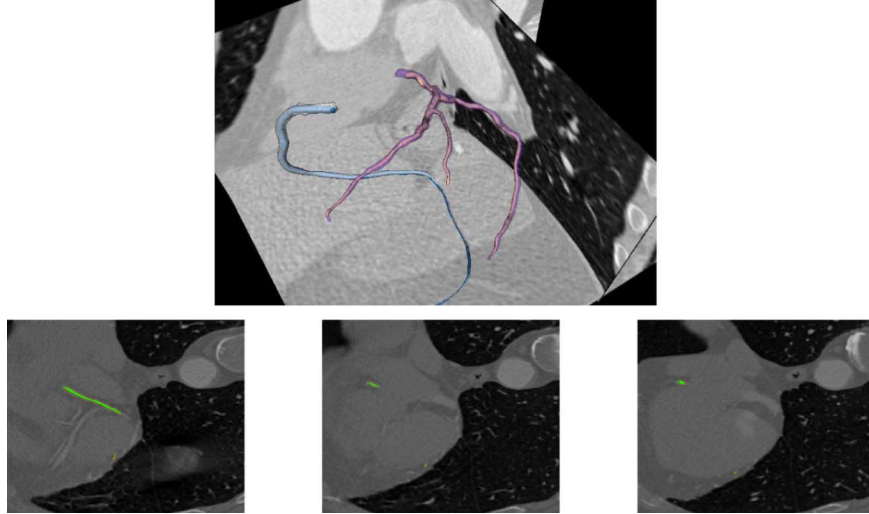


Fig. 16. Visualization of results from experiments for quantitative validation using the Rotterdam cardiac data set [66] (Sample case 1): Top row shows 3-D visualization with ground truth (blue and peach) and corresponding vessel trees segmented by proposed framework (white and magenta), bottom row shows slice-wise visualizations of extracted vessel tree (green) and ground truth (red outline) superimposed on the CTA data.

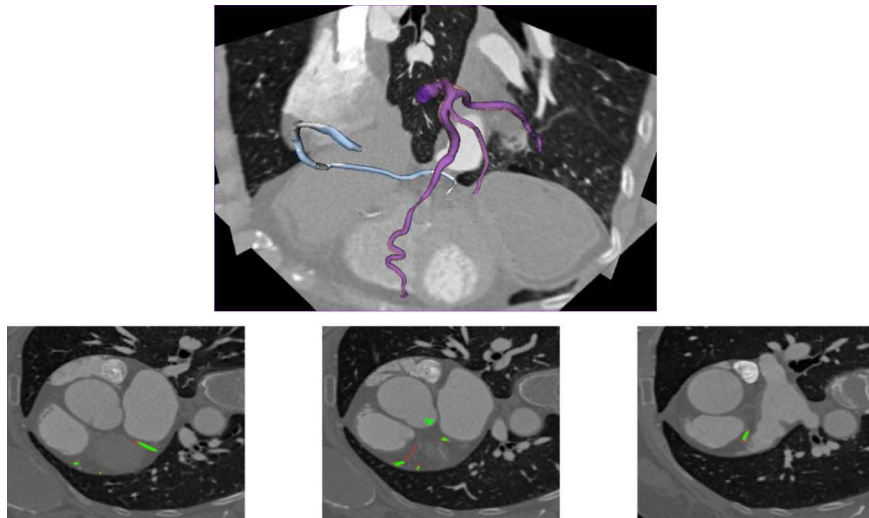


Fig. 17. Visualization of results from experiments for quantitative validation using the Rotterdam cardiac data set [66] (Sample case 2): Top row shows 3-D visualization with ground truth (blue and peach) and corresponding vessel trees segmented by proposed framework (white and magenta), bottom row shows slice-wise visualizations of extracted vessel tree (green) and ground truth (red outline) superimposed on the CTA data.

where Ψ is a function of $p = (x, r) \in \mathbb{R}^4$ and $v \in \mathbb{S}^2$, \tilde{s} is arclength parameter of the curve \tilde{c} . Letting \tilde{c} be time-varying, we can compute the variation of E

$$\frac{d}{dt} E = \int_0^1 \left(\Psi_p \cdot \tilde{c}_t + \Psi_v \cdot \frac{d}{dt} \frac{c'(u)}{|c'(u)|} \right) |\tilde{c}_u| + (\Psi \tilde{c}_{t\tilde{s}} \cdot \tilde{c}_{\tilde{s}} |\tilde{c}_u|) du \quad \frac{d}{dt} E = \int_0^1 \tilde{c}_t \cdot \left[\Psi_p - \frac{\partial}{\partial \tilde{s}} \left(\hat{\Psi}_v \sqrt{1 + \left(\frac{r_{\tilde{s}}}{|c_{\tilde{s}}|} \right)^2} + \Psi \tilde{c}_{\tilde{s}} \right) \right] d\tilde{s}$$

where $\hat{\Psi}_v = (\Psi_v, 0)^T$. Therefore,

$$\frac{1}{L} \nabla_{L^2} E(\check{c}) = \Psi_p - \frac{\partial}{\partial \check{s}} \left(\hat{\Psi}_v \sqrt{1 + \left(\frac{r_{\check{s}}}{|c_{\check{s}}|} \right)^2} + \Psi \check{c}_{\check{s}} \right). \quad (27)$$

The Sobolev gradient is then computed using (25) and (27) yielding

$$\begin{aligned} \nabla_{\text{Sob}} E &= K(\nabla_{L^2} E) \\ &= L \cdot K(\Psi_p) + L \cdot \partial_{\check{s}} K(\hat{\Psi}_v \sqrt{1 + \left(\frac{r_{\check{s}}}{|c_{\check{s}}|} \right)^2} + \Psi \check{c}_{\check{s}}) \end{aligned} \quad (28)$$

where the expressions for the operators $K()$ and $\partial_{\check{s}} K()$ are given in (25) and (26), and they can be computed using formulas (23), (22), and (24).

ACKNOWLEDGMENT

The authors would like to thank M. Kubicki and A. Stillman for their valuable inputs.

REFERENCES

- [1] M. Kass, A. P. Witkin, and D. Terzopoulos, "Snakes: Active contour models," *Int. J. Comput. Vis.*, vol. 1, no. 4, pp. 321–331, 1988.
- [2] V. Caselles, R. Kimmel, and G. Sapiro, "Geodesic active contours," *Int. J. Comput. Vis.*, vol. 22, no. 1, pp. 61–79, 1997.
- [3] S. Kichenassamy, A. Kumar, P. Olver, A. Tannenbaum, and A. Yezzi, "Conformal curvature flows: From phase transitions to active vision," *Arch. Rational Mech. Anal.*, vol. 134, no. 3, pp. 275–301, 1996.
- [4] T. Chan and L. Vese, "Active contours without edges," *IEEE Trans. Image Process.*, vol. 10, no. 2, pp. 266–277, Feb. 2001.
- [5] S. Lankton and A. Tannenbaum, "Localizing region-based active contours," *IEEE Trans. Image Process.*, vol. 17, no. 11, pp. 2029–2039, Nov. 2008.
- [6] J. Kim, J. Fisher, III, A. Yezzi, M. Cetin, and A. Willsky, "A non-parametric statistical method for image segmentation using information theory and curve evolution," *IEEE Trans. Image Process.*, vol. 14, no. 10, pp. 1486–1502, Oct. 2005.
- [7] A. Yezzi, A. Tsai, and A. Willsky, "A statistical approach to snakes for bimodal and trimodal imagery," in *Int. Conf. Comput. Vis.*, Oct. 1999, pp. 898–903.
- [8] M. Rousson, T. Brox, R. Deriche, I. Proje Odyssee, and F. Sophia-Antipolis, "Active unsupervised texture segmentation on a diffusion based feature space," in *Proc. 2003 IEEE Comput. Soc. Conf. Comput. Vis. Pattern Recognit.*, 2003, vol. 2.
- [9] J. Malcolm, Y. Rathi, and A. Tannenbaum, "A graph cut approach to image segmentation in tensor space," in *Proc. IEEE Comput. Soc. Conf. Comput. Vis. Pattern Recognit.*, 2007, pp. 1–8.
- [10] N. Paragios and R. Deriche, "Geodesic active regions and level set methods for supervised texture segmentation," *Int. J. Comput. Vis.*, vol. 46, no. 3, pp. 223–247, 2002.
- [11] V. Mohan, J. Melonakos, A. Tannenbaum, M. Niethammer, and M. Kubicki, "Finsler level set segmentation for imagery in oriented domains," in *Proc. Br. Mach. Vis. Conf.*, 2007, pp. 1–8.
- [12] D. Cremers, M. Rousson, and R. Deriche, "A review of statistical approaches to level set segmentation: Integrating color, texture, motion and shape," *Int. J. Comput. Vis.*, vol. 72, no. 2, pp. 195–215, 2007.
- [13] S. Dambreville, Y. Rathi, and A. Tannenbaum, "A framework for image segmentation using shape models and kernel space shape priors," *IEEE Trans. Pattern Anal. Mach. Intell.*, vol. 30, no. 8, pp. 1385–1399, Aug. 2008.
- [14] J. Malcolm, Y. Rathi, and A. Tannenbaum, "Graph cut segmentation with nonlinear shape priors," in *Proc. IEEE Int. Conf. Image Process.*, 2007, vol. 4, pp. 365–368.
- [15] D. Nain, A. Yezzi, and G. Turk, "Vessel segmentation using a shape driven flow," *Lecture Notes in Computer Science*, pp. 51–59, 2004.
- [16] T. Cootes *et al.*, "Active appearance models," *IEEE Trans. Pattern Anal. Mach. Intell.*, vol. 23, no. 6, pp. 681–685, 2001.
- [17] V. Mohan, G. Sundaramoorthi, J. Melonakos, M. Niethammer, M. Kubicki, and A. Tannenbaum, "Tubular surface evolution for segmentation of the cingulum bundle from DW-MRI," in *Proc. MFCA'08*, 2008, p. 150.
- [18] V. Mohan, G. Sundaramoorthi, A. Stillman, and A. Tannenbaum, "Vessel segmentation with automatic centerline extraction using tubular tree segmentation," in *Proc. MICCAI Cardiovascular Interventional Imag. Biophys. Modell. Workshop*, 2009, pp. 1–8.
- [19] J. Schmahmann and D. Pandya, *Fiber Pathways of the Brain*. New York: Oxford Univ. Press, 2006.
- [20] M. Kubicki, C. Westin, P. Nestor, C. Wible, M. Frumin, S. Maier, R. Kikinis, F. Jolesz, R. McCarley, and M. Shenton, "Cingulate fasciculus integrity disruption in schizophrenia: A magnetic resonance diffusion tensor imaging study," *Biol. Psychiatry*, vol. 54, no. 11, pp. 1171–1180, 2003.
- [21] F. Wang, Z. Sun, L. Cui, X. Du, X. Wang, H. Zhang, Z. Cong, N. Hong, and D. Zhang, "Anterior Cingulum abnormalities in male patients with schizophrenia determined through diffusion tensor imaging," *Am. Psychiatric Assoc.*, vol. 161, pp. 573–575, 2004.
- [22] S. Mori, B. Crain, V. Chacko, and P. van Zijl, "Three dimensional tracking of axonal projections in the brain by magnetic resonance imaging," *Ann. Neurol.*, vol. 45, no. 2, pp. 265–269, 1999.
- [23] T. Conturo, N. Lori, T. Cull, E. Akbudak, A. Snyder, J. Shimony, R. McKinstry, H. Burton, and M. Raichle, "Tracking neuronal fiber pathways in the living human brain," *Proc. Nat. Acad. Sci USA*, vol. 96, no. 18, pp. 10 422–10 427, 1999.
- [24] M. Perrin, C. Poupon, Y. Cointepas, B. Rieul, N. Golestani, C. Pallier, D. Rivière, A. Constantinesco, D. L. Bihan, and J.-F. Mangin, "Fiber tracking in q-ball fields using regularized particle trajectories," in *IPMI*, G. E. Christensen and M. Sonka, Eds. New York: Springer, 2005, vol. 3565, Lecture Notes in Computer Science, pp. 52–63.
- [25] G. J. M. Parker, C. A. M. Wheeler-Kingshott, and G. J. Barker, "Estimating distributed anatomical brain connectivity using fast marching methods and diffusion tensor imaging," *IEEE Trans. Med. Imag.*, vol. 21, no. 5, pp. 505–512, May 2002.
- [26] O. Friman, G. Farneback, and C.-F. Westin, "A Bayesian approach for stochastic white matter tractography," *IEEE Trans. Med. Imag.*, vol. 25, no. 8, pp. 965–978, Aug. 2006.
- [27] C. Lenglet, M. Rousson, R. Deriche, O. D. Faugeras, S. Lehericy, and K. Ugurbil, "A riemannian approach to diffusion tensor images segmentation," in *IPMI*, G. E. Christensen and M. Sonka, Eds. New York: Springer, 2005, vol. 3565, Lecture Notes in Computer Science, pp. 591–602.
- [28] E. Prados, S. Soatto, C. Lenglet, J.-P. Pons, N. Wotawa, R. Deriche, and O. D. Faugeras, "Control theory and fast marching techniques for brain connectivity mapping," in *Proc. IEEE Comput. Soc. Conf. Comput. Vis. Pattern Recognit.*, 2006, pp. 1076–1083.
- [29] F. Zhang, C. Goodlett, E. R. Hancock, and G. Gerig, "Probabilistic fiber tracking using particle filtering," in *MICCAI (2)*, N. Ayache, S. Ourselin, and A. J. Maeder, Eds. New York: Springer, 2007, vol. 4792, Lecture Notes in Computer Science, pp. 144–152.
- [30] J. Cohen-Adad, M. Descoteaux, S. Rossignol, R. D. Hoge, R. Deriche, and H. Benali, "Detection of multiple pathways in the spinal cord white matter using q-ball imaging," in *IEEE Int. Symp. Biomed. Imag.: From Nano to Macro*, May 2008, pp. 696–699.
- [31] C. Xu, D. L. Pham, and J. L. Prince, "Finding the brain cortex using fuzzy segmentation, isosurfaces, and deformable surface models," in *IPMI*, J. S. Duncan and G. Gindi, Eds. New York: Springer, 1997, vol. 1230, Lecture Notes in Computer Science, pp. 399–404.
- [32] A. J. Yezzi, S. Kichenassamy, A. Kumar, P. J. Olver, and A. Tannenbaum, "A geometric snake model for segmentation of medical imagery," *IEEE Trans. Med. Imag.*, vol. 16, no. 2, pp. 199–209, Apr. 1997.
- [33] C. Lenglet, M. Rousson, and R. Deriche, "Dti segmentation by statistical surface evolution," *IEEE Trans. Med. Imag.*, vol. 25, no. 6, pp. 685–700, Jun. 2006.
- [34] Z. Wang and B. C. Vemuri, "Dti segmentation using an information theoretic tensor dissimilarity measure," *IEEE Trans. Med. Imag.*, vol. 24, no. 10, pp. 1267–1277, Oct. 2005.
- [35] S. P. Awate, H. Z. 0005, and J. C. Gee, "Fuzzy nonparametric dti segmentation for robust cingulum-tract extraction," in *MICCAI (1)*, N. Ayache, S. Ourselin, and A. J. Maeder, Eds. New York: Springer, 2007, vol. 4791, Lecture Notes in Computer Science, pp. 294–301.

- [36] J. Melonakos, V. Mohan, M. Niethammer, K. Smith, M. Kubicki, and A. Tannenbaum, "Finsler tractography for white matter connectivity analysis of the cingulum bundle," in *Proc. MICCAI*, 2007, pp. 36–43.
- [37] J. Melonakos, M. Niethammer, V. Mohan, K. Smith, M. Kubicki, and A. Tannenbaum, "Locally-constrained region-based methods for DW-MRI segmentation," in *Proc. IEEE 11th Int. Conf. Comput. Vis.*, 2007, pp. 1–8.
- [38] I. Eckstein, D. Shattuck, J. Stein, K. McMahon, G. de Zubicaray, M. Wright, P. Thompson, and A. Toga, "Active fibers: Matching deformable tract templates to diffusion tensor images," *Neuroimage*, vol. 47, pp. 82–89, 2009.
- [39] L. M. Lorigo, W. E. L. Grimson, O. D. Faugeras, R. Keriven, R. Kikinis, A. Nabavi, and C.-F. Westin, "Codimension—Two geodesic active contours for the segmentation of tubular structures," in *Proc. IEEE CVPR*, 2000, pp. 1444–1451.
- [40] A. Vasilevskiy and K. Siddiqi, "Flux maximizing geometric flows," *IEEE Trans. Pattern Anal. Mach. Intell.*, vol. 24, no. 12, pp. 1565–1578, Dec. 2002.
- [41] D. Nain, A. J. Yezzi, and G. Turk, "Vessel segmentation using a shape driven flow," in *MICCAI (1)*, C. Barillot, D. R. Haynor, and P. Hellier, Eds. Springer: Springer, 2004, vol. 3216, Lecture Notes in Computer Science, pp. 51–59.
- [42] R. Manniesing, B. Velthuis, M. van Leeuwen, I. van der Schaaf, P. van Laar, and W. Niessen, "Level set based cerebral vasculature segmentation and diameter quantification in CT angiography," *Med. Image Anal.*, pp. 200–214, 2006.
- [43] H. Li and A. Yezzi, "Vessels as 4-D curves: Global minimal 4-D paths to extract 3-D tubular surfaces and centerlines," *IEEE Trans. Med. Imag.*, vol. 26, pp. 1213–1223, 2007.
- [44] L. D. Cohen and R. Kimmel, "Global minimum for active contour models: A minimal path approach," in *Proc. IEEE CVPR*, 1996, pp. 666–673.
- [45] S. Bouix, K. Siddiqi, and A. Tannenbaum, "Flux driven automatic centerline extraction," *Med. Image Anal.*, vol. 9, no. 3, pp. 209–221, 2005.
- [46] T. Binford, "Visual perception by computer," in *IEEE Conf. Syst. Control*, 1971, vol. 261.
- [47] T. O'Donnell, M. Dubuisson-Jolly, and A. Gupta, "A cooperative framework for segmentation using contours and 3-D hybrid models as applied to branching cylindrical structures," in *Proc. 6th Int. Conf. Comput. Vis.*, 1998, p. 454.
- [48] R. Li and S. Ourselin, "Accurate curvilinear modelling for precise measurements of tubular structures," in *Proc. VIIth Biennial Australian Pattern Recognit. Soc. Conf. Digital Image Comput.: Tech. Appl. (DICTA 2003)*, 2003, p. 243.
- [49] A. Frangi, W. Niessen, R. Hoogeveen, T. van Walsum, and M. Viergever, "Model-based quantitation of 3-D magnetic resonance angiographic images," *IEEE Trans. Med. Imag.*, vol. 18, no. 10, pp. 946–956, Oct. 1999.
- [50] J. Montagnat and H. Delingette, "4D deformable models with temporal constraints: Applications to 4D cardiac image segmentation," *Med. Image Anal.*, vol. 9, no. 1, pp. 87–100, 2005.
- [51] C. van Bommel, O. Wink, B. Verdonck, M. Viergever, and W. Niessen, "Blood pool contrast-enhanced MRA: Improved arterial visualization in the steady state," *IEEE Trans. Med. Imag.*, vol. 22, no. 5, pp. 645–652, May 2003.
- [52] D. Lesage, E. Angelini, I. Bloch, and G. Funka-Lea, "A review of 3-D vessel lumen segmentation techniques: Models, features and extraction schemes," *Med. Image Anal.*, pp. 819–845, 2009.
- [53] C. Florin, N. Paragios, and J. Williams, "Particle filters, A quasi-Monte Carlo solution for segmentation of coronaries," in *Med. Image Comput. Computer-Assisted Intervent. (MICCAI 2005)*, 2005, pp. 246–253.
- [54] G. Agam and C. Wu, "Probabilistic modeling based vessel enhancement in thoracic CT scans," in *IEEE Comput. Soc. Conf. Comput. Vis. Pattern Recognit. (CVPR 2005)*, 2005, vol. 2.
- [55] R. Manniesing and W. Niessen, "Local speed functions in level set based vessel segmentation," in *Med. Image Comput. Computer-Assisted Intervent. (MICCAI 2004)*, 2004, pp. 475–482.
- [56] D. Wilson, J. Noble, and N. Csiro, "An adaptive segmentation algorithm for time-of-flight MRA data," *IEEE Trans. Med. Imag.*, vol. 18, no. 10, pp. 938–945, Oct. 1999.
- [57] T. O'Donnell, T. Boulton, X. Fang, and A. Gupta, "The extruded generalized cylinder: A deformable model for object recovery," in *1994 IEEE Comput. Soc. Conf. Comput. Vis. Pattern Recognit. (Proc. CVPR'94)*, 1994, pp. 174–181.
- [58] L. Zhu, S. Haker, and A. Tannenbaum, "Flattening maps for the visualization of multibranching vessels," *IEEE Trans. Med. Imag.*, vol. 24, no. 2, pp. 191–198, Feb. 2005.
- [59] L. Wang and A. Bhalerao, "Model based detection of branching structures," presented at the Med. Image Understand. Anal., Portsmouth, U.K., 2002.
- [60] E. Pichon, C.-F. Westin, and A. Tannenbaum, "Anisotropic conformal flows and DT-MRI tractography," in *Proc. MICCAI*, 2005, pp. 1–7.
- [61] E. Pichon, "Novel methods for multidimensional image segmentation," Ph.D. dissertation, Georgia Inst. Technol., Atlanta, 2005.
- [62] J. Melonakos, E. Pichon, S. Angenent, and A. Tannenbaum, "Finsler active contours," *IEEE Trans. Pattern Anal. Mach. Intell.*, vol. 30, no. 3, pp. 412–423, 2008.
- [63] G. Sundaramoorthi, A. J. Yezzi, A. Mennucci, and G. Sapiro, "New possibilities with Sobolev active contours," in *Proc. SSVM*, 2007, pp. 153–164.
- [64] T. Kanungo, D. Mount, N. Netanyahu, C. Piatko, R. Silverman, and A. Wu, "An efficient k-means clustering algorithm: Analysis and implementation," *IEEE Trans. Pattern Anal. Mach. Intell.*, pp. 881–892, 2002.
- [65] J. Hartigan and M. Wong, "A K-means clustering algorithm," *JR Stat. Soc. Ser. C-Appl. Stat.*, vol. 28, pp. 100–108, 1979.
- [66] M. Schaap *et al.*, "Standardized evaluation methodology and reference database for evaluating coronary artery centerline extraction algorithms," *Med. Image Anal.*, vol. 13, no. 5, pp. 701–714, 2009.
- [67] V. Mohan, G. Sundaramoorthi, M. Kubicki, D. Terry, and A. Tannenbaum, "Population analysis of the cingulum bundle using the tubular surface model for schizophrenia detection," in *Proc. SPIE Med. Imag.*, 2010, vol. 7624, pp. 1–8.
- [68] G. E. Christensen, *Information Processing in Medical Imaging, 19th International Conference*. New York: Springer, 2005, vol. 3565, Lecture Notes in Computer Science.